Characterization of porosity in a 19th century painting ground by synchrotron radiation X-ray tomography

**Claire Gervais · Jaap J. Boon · Federica Marone ·
Ester S.B. Ferreira**

Abstract The study of the early oeuvre of the Swiss painter Cuno Amiet (1868–1961) has revealed that, up to 1907, many of his grounds were hand applied and are mainly composed of chalk, bound in protein. These grounds are not only lean and absorbent, but also, as Synchrotron radiation X-ray microtomography has shown, porous. Our approach to the characterization of pore structure and quantity, their connectivity, and homogeneity is based on image segmentation and application of a clustering algorithm to high-resolution X-ray tomographic data. The issues associated with the segmentation of the different components of a ground sample based on X-ray imaging data are discussed. The approach applied to a sample taken from "Portrait of Max Leu" (1899) by Amiet revealed the presence of three sublayers within the ground with distinct porosity features, which had not been observed optically in cross-section. The upper and lower layers are highly porous with important connectivity and thus prone to water uptake/storage. The middle layer however shows low and nonconnected porosity at the resolution level of the X-ray tomography images, so that few direct water absorption paths through the entire sample exist. The potential of the method to characterize porosity and to understand moisture-related issues in paint layer degradation are discussed.

1 Introduction

The build-up of canvas paintings can be complex in composition and layering. The support (for example, a canvas made of hemp, flax, cotton, or a mixture thereof) is often prepared with a layer of size (applied as a diluted collagen aqueous solution), sealing the canvas and smoothing the fiber profile. A ground layer is then normally applied onto it, to provide a smooth even surface for preparatory drawing and painting. Multiple layers of paint are then applied, and the surface can be finished with a varnish layer. The properties of ground layers can vary with the composition and application technique. In the case of the Swiss painter Cuno Amiet (1868–1961), the grounds of paintings he created between 1892 and 1907 are often hand applied. In the vast majority of cases, these are calcium carbonate grounds bound in proteinaceous binder, which have a very porous appearance, are lean in composition and thus absorbent. This kind of ground is required when the artist wants to use a faster working technique and/or desires a matt surface appearance. How porous are these so-called absorbent grounds? What is their storage capacity for binding medium constituents of subsequent paint layers? Can porous grounds be reservoirs for moisture or other solvents from conservation treatments? Is it possible that a moisture gradient within the painting multilayered system (i.e., paints, ground, size, and canvas) will promote the formation and the transport of mobile components, especially upon aqueous treatments or in a noncontrolled display

C. Gervais · J.J. Boon · E.S.B. Ferreira (✉)
Swiss Institute for Art Research (SIK-ISEA), Zollikerstrasse 32, 8032 Zürich, Switzerland
e-mail: ester.ferreira@sik-isea.ch
Fax: +41-44-3815250

Present address:
C. Gervais
Bern University of the Arts, Fellerstrasse 11, 3027 Bern, Switzerland

J.J. Boon
JAAP Enterprise for MOLART Advice, Nieuwendammerdijk 79, 1025LD Amsterdam, The Netherlands

F. Marone
Swiss Light Source (SLS), Paul Scherrer Institute, Villigen, Switzerland

or storage environment? All these questions are still open, and the answers could definitely shed more light on some of the degradation processes observed in paintings.

Evidence of material mobility has been observed in ground and paint layers. The mobile phase in paints consists typically of substances that are not covalently bound to the cross-linked aged paint network.

It has been shown that in oil bound paints and grounds, a large percentage of the glycerol ester bonds have suffered hydrolysis releasing mobile components such as diacids, saturated fatty acids, and glycerol [3, 23]. Evidence of the presence of these mobile phases, often in the form of metal soaps, has been detected in samples from old master's paints and ground layers [11, 18, 24]. In a recently published study [8], it was shown that the porous, absorbent nature of the ground layer played an important role in the formation and agglomeration of calcium soaps in the painting "Autumn in Oschwand" by Cuno Amiet dating from 1906. Other sources of mobile components have been reported, for example, the formation of water soluble arsenic trioxide as a degradation product of the pigments copperacetoarsenite (Emerald green), orpiment and realgar [12]. The investigation of the role of the preparation layers in the formation and transport of these materials is our main research question. Synchrotron x-ray microtomography has been successfully applied to the study, without sample manipulation, of internal features of a vast number of materials including, for example, metal [13, 14], bone [25], microfossils [6], stone [1], ceramic [15], plant tissue [17, 22], and cement samples [9]. In an earlier paper [7], we have reported on the use of synchrotron x-ray tomographic microscopy (SRXTM) to visualize the porosity of painting grounds. The observation of large voids in a matrix with a finer and more complex pore distribution in these ground layers lead to the question of how these pores are connected and what role they play in water storage and material transport.

In this paper, we discuss particularly the procedure implemented to process SRXTM data and extract new information on the porosity including quantitative aspects and connectivity. Comparison with Scanning Electron Microscopy (SEM) images allows discussing the pros and cons of both methods in visualizing porous grounds.

2 Experimental

2.1 Sample

The sample was collected from the edge of Cuno Amiet's painting *Portrait of Max Leu* (1898) (Fig. 1). It consists in a ground sample of size 700 μm length × 500 μm, with no paint layer present at the top. Bulk analysis (FTIR) showed it to be a calcium carbonate ground bound with a proteinaceous medium. Traces of clay minerals were also found.

2.1.1 Preparation of cross-sections

For cross-section preparation, the sample was coated with a 10 nm gold layer (to reduce resin penetration in the sample), embedded in Technovit LC 2000 and polished on Micromesh sheets up to grade 12000. Surface improvement with ion polishing was carried out on the JEOL cross-section polisher using a 5 kV Argon ion beam [2].

2.2 Analytical methods

2.2.1 SEM

Scanning Electron Microscopy (SEM) was performed on an XL30 FEG high-vacuum electron microscope. The sample was gold coated (2 nm). Secondary electron (SE) images were collected at 2 kV spot size setting 3 (corresponding to a beam diameter 1.7 nm) working distance (WD) 5.1 mm and Backscattered Electron (BSE) at 10 kV spot size 3 (beam diameter 2.4 nm) WD 5.1 mm.

Fig. 1 Cuno Amiet, Portrait of Max Leu, 1898, oil on canvas, 73.5 × 84 cm, Kunstmuseum Solothurn (Copyright Daniel Thalmann. Reproduced with permission) and detail of the ground layer on the lower edge of the painting, scale in mm
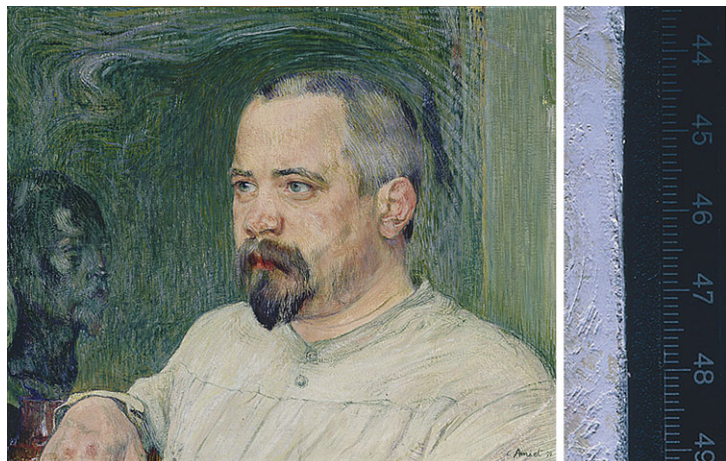
2.2.2 FTIR

Subsamples were analyzed by Fourier Transform Infrared Spectroscopy. FTIR was performed in a Perkin Elmer Fourier Transform Infrared Microspectrometer (Perkin Elmer System 2000) with IR/VIS microscope (Perkin Elmer i-series). Samples were analyzed in a diamond cell.

2.3 Synchrotron radiation X-ray tomographic microscopy (SRXTM)

The sample was attached to the sample holder with the aid of epoxy resin. The sample holder consists of a 32-mm-long steel flat top rod, 500-μm wide at the sample level fixed onto an aluminium base. Microtomographic scans were performed at the TOMCAT beamline of the Swiss Light Source (SLS) in Villigen (Switzerland) [21]. For each tomographic scan, 1501 projections over 180° were acquired (resulting in an angular step of 0.12°). For optimal contrast, the energy was set to 17 keV, and the exposure time per projection was 200 ms. During measurement, the sample was cooled using a cryojet to a temperature of 233 K to minimize beam damage to the sample and epoxy resin. Images were magnified using a 20× optical objective resulting in a pixel size of 0.37 μm. Tomographic reconstructions were computed using a highly optimized routine based on the Fourier transform method [16]. The reconstructed data cube of images had an 8-bit resolution, i.e., with voxels having a greyscale value ranging from 0 (dark: non absorbing material) to 255 (white: highly absorbing material). They were processed and analyzed with the commercial software Avizo 7.0.

2.4 Processing of SRXTM images

A first look at the SRXTM images shows that the sample is composed of two types of empty spaces: (i) large spherical pores ranging from a few microns to 50 microns in width and (ii) a porosity network featuring small pores of undefined shapes (of micron-size) interconnected to each other. Hereafter, voids refer to empty spaces in the sample; large pores refer to well-defined empty voids with a spherical shape.

Two methods were applied to process the SRXTM images, depending whether the goal was to visualize the distribution of the large pores in the whole sample or to analyze the entire porosity network and specifically its connectivity.

2.4.1 Visualization of the distribution of large pores

A representative picture of the distribution of the large pores was obtained by imaging them over the entire sample volume. The size of the entire 3D SRXTM image is large (2048 × 2048 × 2040 voxels, i.e., 8 GB file) and image processing such as filtering requires two to three times more

memory than the image file. This was not possible with our current software package/workstation setup. Therefore, the procedure described hereafter was applied on raw unfiltered greyscale images. The visualization procedure consisted of segmenting the pores by means of the region-growing algorithm. This segmentation procedure is relatively insensitive to noise and allows for an easy segmentation of materials well defined by clear edges. The procedure consists of selecting a set of "seed voxels" corresponding to the material or property of interest and growing regions from these seeds. In our case, we are interested in selecting the pores, represented by low greyscale values (see discussion below on the interpretation of the greyscale histogram in the paragraph "Determination of the segmentation threshold"). We defined seed voxels as all the voxels with a greyscale value below 60. The regions are then grown with a growth rate depending on the greyscale values of the encountered voxels. The higher the greyscale difference to the seed voxels, the slower the growth. This procedure allows stopping the selection efficiently at the edges. The region-growth algorithm was found efficient in visualizing the large spherical pores and allowed a good comparison of the different porosity regions present in the sample (see Fig. 2). However, visual inspection at microscale showed that a large part of the porosity network was not selected. One reason could be that channels constituting the porous network are narrow regions with less well-defined edges. In these channels, voxels have typically higher grey values (i.e., >60) and are thus not selected as seeds. As well, noise (defined by a few voxels with higher greyscale value) may stop the growth too early, resulting in the nonselection of these regions [19]. In conclusion, this procedure based on region-growing algorithm on unfiltered grayscale images is sufficient to visualize the gen-
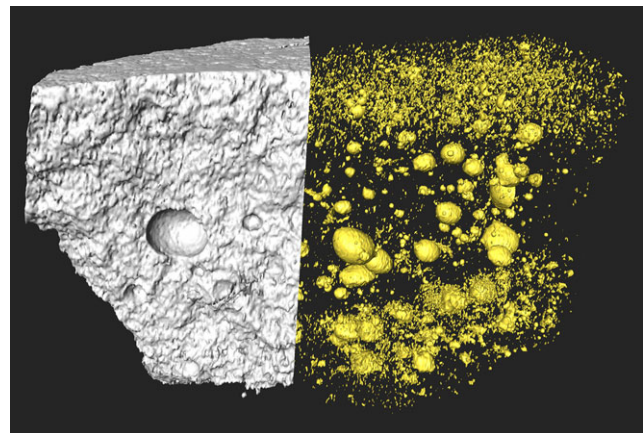

Fig. 2 Details of the porosity of the ground layer of Cuno Amiet's "Portrait of Max Leu". Size in length: 700 μm. *Top* of the *image* corresponds to the top of the ground sample. *Left*: surface of the sample. *Right*: pores present in the structure. For clarity, only pores with a volume larger than 27 voxels (1.37 μm^3) are represented

eral distribution of the large pores but does not allow a correct analysis of the connectivity of the porous network.

2.4.2 Analysis of the connectivity in the porous network

In view of these findings, we used another segmentation procedure to analyze the connectivity of the entire porosity network. The sequence of image processing steps consisted of (i) filtering the SRXTM images to remove noise, (ii) segmentation into pore and nonpore voxels, and (iii) analyzing the pore distribution and connectivity of the 3D porous system by means of an in-house algorithm.

(i) Filtering intends to remove noise that could hinder a correct segmentation of the images. It was performed using a 3D edge-preserving smoothing algorithm provided in the Avizo software. This algorithm combines Gaussian smoothing and anisotropic diffusion, and efficiently removes background noise while keeping sharp edges. Optimal parameters for the entire samples were found to be [time stop: 10; time step: 1; contrast: 8; sigma: 2]. Note that these parameters must be evaluated and reassessed for each image set. A basic test for the correctness of the filtering (which should remove noise but not information about the material itself) consists of subtracting greyscale values between raw and filtered images. The resulting image difference should contain only noise, and no precise shape of the different objects (e.g., calcite crystals) should be visible.

(ii) Segmentation consists of partitioning the image in different sets of voxels, each set representing a different object or material. In our case, the goal is to extract the pores from the ground matrix which can be simply achieved by greyscale thresholding. Indeed, as shown later, the pores have low greyscale values distinct from the binding medium and the calcite composing the ground matrix. The threshold value selected was 86. All voxels below or equal to this value were attributed to pores, the rest being considered as ground matrix.

(iii) The analysis of the porosity was performed on the segmented 3D binary images and consisted of looking at the total porosity and the connectivity of the porous network. The total porosity was calculated by the ratio $n_{pores}/(n_{pores} + n_{ground})$ with n_{pores} and n_{ground} the total number of voxels attributed to pores and ground matrix, respectively. To analyze the connectivity in our sample, we define a cluster as a set of all the voxels connected to each other. Voxels are considered to be connected if they are nearest neighbors, i.e., if they share a common face. The spatial and size distribution of all the independent clusters present in the sample can then be analyzed. We used the Hoshen–Kopelman (HK) algorithm [10] to count and label all the independent clusters within our 3D binary image. Based on the union-find data structure [5], the HK algorithm is an efficient means to enumerate independent clusters within a single scan through the voxel grid.

3 Results and discussion

3.1 Validation of the image processing procedure

The validation of the image processing was performed in two steps. The first step consisted in attributing greyscale values found in the histogram to the different materials constituting the ground and determining the optimal threshold value to segment the porous network. The second step focused on a detailed comparison between SRXTM and SEM data of a target slice chosen in the sample. The target slice was chosen to contain a series of features of interest, such as foraminifera, a large silica rich particle, a number of large voids, a significant pore distribution, and penetrating epoxy resin [7]. The comparison between the SRXTM and SEM target slices permits the discussion, on the one hand, of the suitability and limits of both methods for the study of porosity and, on the other hand, of the validity of the filtering and segmentation processes.

3.1.1 Determination of the segmentation threshold

Figure 3 shows the image processing procedure applied to the sample. The greyscale histogram of the raw data (Fig. 3a, bottom) shows the presence of two narrow peaks centered at 75 and 83 values and a large distribution of greyscale values in the upper region. After filtering (Fig. 3b), the separation of the two peaks at lower greyscale values is enhanced, and the shape of the broader band at higher greyscale values hints at a bimodal distribution centered around 140 and 200. Comparison of the images before and after filtering (Figs. 3a and 3b) shows that the edge and small details are still visible. Therefore, the filtering efficiently highlights the greyscale differences without removing or altering details of the image. The attribution of the greyscale regions to different materials was performed with the ground composition in mind. FTIR has shown that the ground was composed mainly of chalk, protein, and a small amount of clay minerals with a kaolin-type infrared spectrum. Considering the attenuation coefficients of those different materials and their respective proportion on the SRXTM images, we made the following attribution: The two lower greyscale groups were defined to be empty space. Voxels in these groups are those of the external space, the large pores, and the porous network of the sample. The third greyscale group centered at 140 may be mainly attributed to binding medium, while the last region to large calcite and silicate crystals.
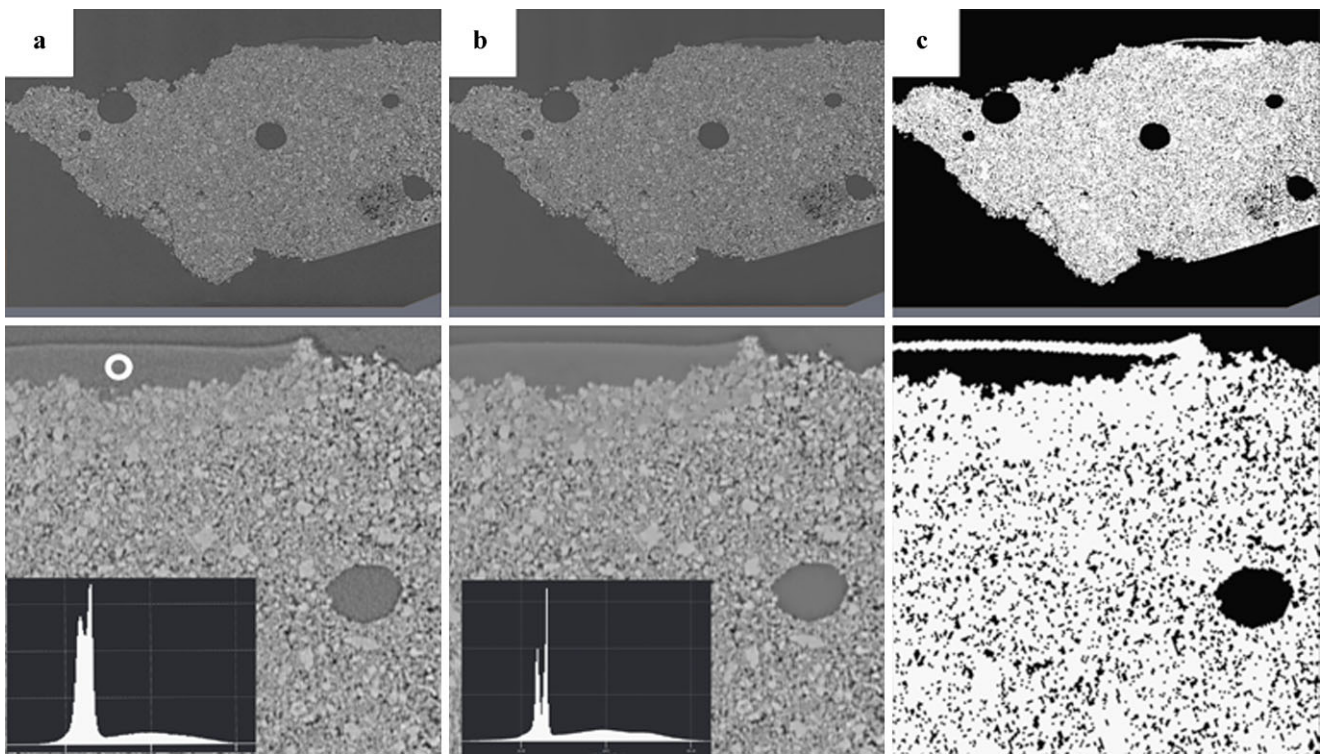
Fig. 3 Image processing procedure (filtering and segmentation) applied to the target slice. (**a**) Raw image. The *circle* indicates the location of the epoxy resin used to fix the sample to the holder. (**b**) Filtered image. (**c**) Segmented image

Using a threshold value of 86 (Fig. 3c), the larger pores and the external space to the sample are correctly segmented. It must be mentioned that at a threshold value of 86, the interior of the epoxy resin drop (Fig. 3c detail) is inaccurately selected as a void space suggesting that there is some overlap in the greyscale value distribution between voids and organic matter (resin and binding medium).

The bimodal distribution of the voids could be explained by edge-enhancement effects. The formation of Fresnel fringes is described theoretically and experimentally by Snigirev et al. [20] and phase contrast imaging explored by Cloetens et al. [4]. This artefact happens when X-rays cross edges between two materials of different refraction indices, such as void and calcite here. As a result, the pixels near the material borders have an increased contrast, i.e., the void regions near material edges seem darker than they should be.

Concluding, it seems reasonable to select both peaks in the segmentation (threshold value 86) to provide a more accurate representation of porosity, i.e., including both the porous network and the larger pores accepting the slight overestimation of the overall porosity due to the overlap between the greyscale range of the organic resin or proteinaceous medium and the empty pore space.

3.1.2 Comparison between SEM and SRXTM data

After the tomography measurements, the sample was embedded and polished to expose the target slice [7]. The cross-section was then studied by SEM in electron backscattering mode (BSE, Fig. 4d) and secondary electron mode (SE, Fig. 4e) for comparison with the SRXTM target slice (Fig. 4a and detail 4b) and the corresponding segmented image (Fig. 4c).

We will concentrate our comparison between SEM and SRXTM slices on three features: the large pores (* in Fig. 4d), the foraminiferous fossils (♦ in Fig. 4d), and the very fine calcite particles distributed within the binding medium.

Large pores SRXTM data show the presence of empty large pores (Fig. 4b, top), which possibly originate from trapped air bubbles formed after the application of the ground layer. These look deformed and filled with "debris" in the SEM-BSE image (* in Fig. 4d). This difference may be attributed to the polishing process that can redistribute calcite and binding medium particles and redeposit them in the large voids, totally or partially filling them. Thus, the SEM image of the target slice does not, in this case, correctly visualize the porosity due to artefacts introduced during surface preparation, namely the redistribution of calcite particles [7].
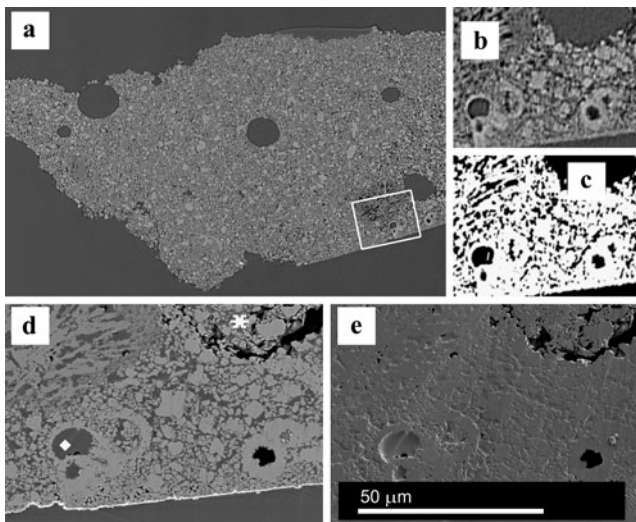
Fig. 4 (**a**) Target slice chosen to compare SRXTM and SEM images. (**b**) Raw and (**c**) segmented SRXTM image and corresponding. (**d**) SEM-BSE and (**e**) SE images. In image (**d**), the foraminifera (♦) and large pore filled with debris (*) are indicated

Foraminiferous fossils The fossils are seen as empty in the segmented SRXTM target slice but filled with organic film in both SEM-SE and SEM-BSE data [see Figs. 4d (♦) and 4e]. Note that another fossil at the right of the image remains empty whatever the method of visualization. The presence of this organic material within the fossils is more complex to understand, and two main hypotheses can be proposed: (i) the organic film can be proteinaceous binding medium mixed in preparation of the ground substance, or (ii) it may be a result of the cross-section preparation (acrylate resin).

In our case, the foraminiferous fossil chambers are relatively closed in shape; however, the walls of these chambers are porous. These pores can allow the filling up of the chamber during ground preparation (hypothesis (i)). Finally, the organic film could be an artefact from sample preparation prior to SEM. The nature of the material inside the chamber is currently being investigated further by FTIR imaging, to determine if the film is proteinaceous or not.

Very fine calcite particles and binding medium Very fine calcite particles are clearly visible in the SEM images but are shown as an average greyscale region in the SRXTM images (see, e.g., between the two fossils at the bottom of Fig. 4b). This effect is due to the resolution or pixel size of the tomography data, fixed to 370 nm. Any information on particles or pores of smaller dimensions is thus lost. The resulting artefact is called partial volume effect. This effect happens when two materials with different absorption coefficients lie in the same voxel, leading to an average greyscale for that voxel not representative of the reality [19, and references therein]. In our case, the greyscale middle range in the

histogram originally attributed to binding medium is thus likely to contain not only binding medium but also small calcite particles. As a consequence, the partial volume effect would severely hinder a correct segmentation between calcite and binding medium. However, it does not seem to influence the visualization of the porous network. Reassuringly, when looking at a region where some epoxy resin used for mounting the sample prior to tomography has been absorbed within the ground (Fig. 3a), this feature is correctly segmented on the SRXTM target slice, where the region exhibits a much lower porosity (Fig. 3c).

In view of these findings, the proposed procedure based on the segmentation of SRXTM images seems to be able to adequately extract most of the porosity features of the ground. While limited in the visualization of submicron features, it allows getting much information about the ground porosity, its main characteristics, and its 3D topology. Besides, the fact that the sample is tomographed almost without preparation excludes the various artefacts seen on the SEM images related to sample preparation.

3.2 Insight into the ground properties of the painting "Portrait of Max Leu" by Cuno Amiet

A clear difference in type and distribution of porosity is observed throughout the sample (Fig. 2). This complex substructure of the ground, possibly related to multiple layer application, could not be observed in the light microscopy or SEM study of the polished cross-section. The ground can be mainly divided into three sublayers hereafter denominated layers 1, 2, and 3. The top layer (layer 1) is characterized by a very fine porosity, i.e., with large numbers of small pores. The middle layer (layer 2) has less fine pores but exhibits large spherical pores, suggesting these to be air bubbles trapped during the drying process. Finally, the bottom layer (layer 3) is composed of fine pores and a few larger pores. Its lower profile is very rough and can be explained by its contact with the canvas fibers.

To get insight into the connectivity within these three layers, we applied our HK clustering method to a subset composed of $644 \times 1464 \times 932$ voxels. This choice was determined by both computer resources and the need to remove the edges of the sample, which could present a porosity nonrepresentative of the bulk. More than 792,000 clusters were found, with sizes ranging from 1 single voxel to $\sim 52 \times 10^6$ voxels. The total bulk porosity of the sample was estimated to be ~ 15 % (volume fraction). All the exterior voxels were excluded in the porosity calculation. The definition of the exterior is trivial at the upper flat layer, but it becomes however difficult for the bottom layer, which shows a very rough surface. The figure was calculated by excluding all voxels belonging to the xy slices external to the sample [i.e., below slice number 200 (i.e., depth of 74 µm) and
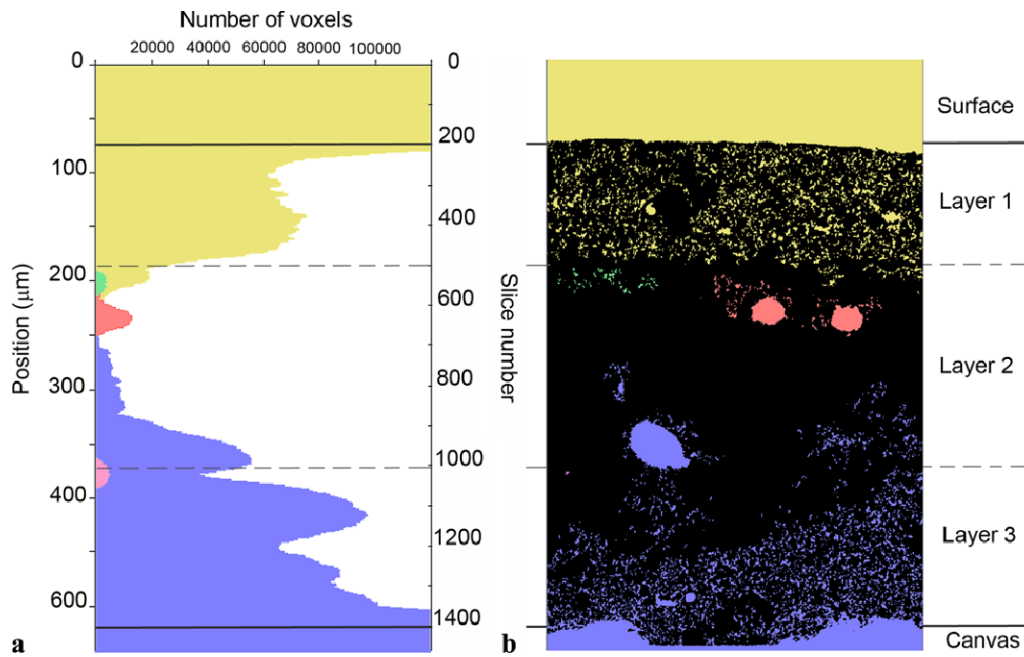
Fig. 5 (**a**) Profile of distribution in depth of the five major porosity connected clusters in the sample (total number of voxels belonging to the cluster for each *xz* slice scanned along the sample). *Solid horizontal lines* show the sample limits, *dashed lines* are an estimate of the interface between the three layers composing the ground. (**b**) Virtual 2D *yz* cross-section of the sample with visualization of the five biggest connected clusters. Note that the connectivity between voxels is not always visible because the connection path is located in the third dimension (*y* axis)

above slice number 1400 (i.e., depth of 518 μm)] (see solid horizontal lines in Fig. 5).

Clusters were then classified according to their size (total number of voxels), and the five biggest clusters were selected for visualization (Fig. 5b). Two clusters are predominant in terms of size and account for 58 % of the total porosity. The other three clusters imaged, third, fourth, and fifth in size only account for a further 1 % of the porosity. The biggest one (yellow) is homogeneously distributed within layer 1, as can be shown by the constant number of voxels found in the *xy* slices composing this layer (Fig. 5a). The second one (blue) is located in layer 3 and shows a significant heterogeneity in its distribution. This heterogeneity results from the presence of very large pores and from the irregular thickness of the bottom layer. In addition, the blue cluster extends into layer 2, so that the layer interface is not as well defined as suggested when looking only at the large pores (Fig. 2). If the different layers correspond to different application steps, this undefined interface could be due to the fact that layer 2 has been applied shortly after layer 3, which was thus not completely dry. The sizes of the third and subsequent clusters are negligible. They represent only local connectivity with either large pores connected to their nearest pore neighbors (e.g., red cluster) or small closed porous regions (green cluster).

The spatial distribution of the clusters confirms the heterogeneous aspect of the sample. It shows that both top

and lower areas of the sample contain open, fully connected porous networks, whereas the middle layer has isolated smaller clusters not connected to the surface or the canvas side of the ground layer. In terms of transport properties, and providing that the level of resolution of the SRXTM images is sufficient to assess the main properties of the porosity network, it means that the ground will effectively absorb both the binding media applied over it and any material applied to the back of the canvas, justifying its definition of an absorbent ground. However, the transport path through the ground, from the back of the painting to the paint layers is not open. Therefore, one can empirically predict that the ground can act as a material reservoir but the transport through it is likely to be slow.

4 Conclusion

SRXTM is a powerful way to visualize porosity within unmanipulated microsamples, avoiding issues relating to sample preparation. The visualization and segmentation of the different components on painting ground samples is greatly assisted by image filtering. It was found that 3D edge preserving smoothing filtering gave adequate results, improving the distinction between the greyscales of the different materials, while not loosing relevant material information. After filtering, the porosity of the sample could be distinguished and segmented. The sample appeared to consist of

large spherical pores (10 to 50 microns wide) and a microporous network featuring small pores of undefined shape interconnected to each other.

Analysis of the porosity distribution and in particular porosity connectivity in the segmented data provided additional information, not clearly visible in the greyscale CT images, nor in the SEM imaging. It was shown that the ground layer of the painting by Cuno Amiet entitled *Portrait of Max Leu* has three layers with distinct porosity properties. The top layer is characterized by a very fine well-connected porosity, whereas the middle layer shows less connectivity but exhibits large spherical pores. Finally, the lower layer is composed of connected small pores and a few large spherical pores. This observation suggests that this ground layer has the capability of absorbing medium from paint layers applied onto it or conservation treatments although limited capability of fast transport through it.

The image analysis approach described here was able to provide unique new information in estimating the main porosity characteristics of a ground layer. Although some issues remain with the detailed accuracy of material segmentation, SRXTM images can provide important information when estimating and comparing the absorbency and transport properties of ground layers of similar composition.

References

1. C.R. Appoloni, C.P. Fernandes, C.R.O. Rodrigues, Nucl. Instrum. Methods Phys. Res. A **580**, 629–632 (2007)
2. J.J. Boon, J. van der Horst, in *Preparation for Painting*, ed. by J.H. Townsend, T. Doherty, G. Heidenreich, J. Ridge (Archetype Publications, London, 2008), pp. 42–50
3. J.J. Boon, S. Peulvé, O.F. van den Brink, M.C. Duursma, D. Rainford, in *Early Italian Paintings: Techniques and Analysis, Symposium*, Maastricht, 9–10 October 1996, ed. by T. Bakkenist, R. Hoppenbrouwers, H. Dubois (Limburg Conservation Institute, Maastricht, 1997), pp. 35–56
4. P. Cloetens, R. Barrett, J. Baruchel, J.-P. Guigay, M. Schlenker, J. Phys. D, Appl. Phys. **29**, 133–146 (1996)
5. T.H. Cormen, C.E. Leiserson, R.L. Rivest, C. Stein, in *Introduction to Algorithms*, 2nd edn. (MIT Press/McGraw–Hill, Cambridge/New York, 2001), pp. 498–524, ISBN 0-262-03293-7. Chap. 21
6. P.C.J. Donoghue, S. Bengtson, X. Dong, N.J. Gostling, T. Huldtgren, J.A. Cunningham, Y. Yin, Z. Yue, F. Peng, M. Stampanoni, Nature **442**(7103), 680–683 (2006)
7. E.S.B. Ferreira, J.J. Boon, J. van der Horst, N.C. Scherrer, F. Marone, M. Stampanoni, in *O3A: Optics for Arts, Architecture, and Archaeology II*, ed. by L. Pezzati, R. Salimbeni (2009)
8. E.S.B. Ferreira, J.J. Boon, M. Stampanoni, F. Marone, in *ICOM-CC Lisbon 2011: Preprints 16th Triennial Conference Lisbon*, ICOM, 2011, Paris, 9–23 September 2011 (2011), pp. 1604 1–8
9. E. Gallucci, K. Scrivener, A. Groso, M. Stampanoni, G. Margaritondo, Cem. Concr. Res. **37**(3), 360–368 (2007)
10. J. Hoshen, R. Kopelman, Phys. Rev. B **14**, 3438–3445 (1976)
11. K. Keune, J.J. Boon, Stud. Conserv. **52**, 161–176 (2007)
12. K. Keune, J.J. Boon, in *ICOM-CC Lisbon 2011: Preprints 16th Triennial Conference Lisbon*, ICOM, 2011, Paris, 19–23 September 2011 (2011), pp. 1609 1–7
13. C. Landron, E. Maire, O. Bouaziz, J. Adrien, L. Lecarme, A. Bareggi, Acta Mater. **59**, 7564–7573 (2011)
14. E. Maire, J. Buffière, L. Salvo, J.J. Blandin, W. Ludwig, J.M. Létang, Adv. Eng. Mater. **3**(8), 539–546 (2001)
15. E. Maire, P. Colombo, J. Adrien, L. Babout, L. Biasetto, J. Eur. Ceram. Soc. **27**, 1973–1981 (2007)
16. F. Marone, M. Stampanoni, J. Synchrotron Radiat. **19**, 1029–1037 (2012)
17. F. Mendonza, P. Verboven, H.K. Mebatsion, G. Kerckhofs, M. Wevers, B. Nicolaï, Planta **226**, 559–570 (2007)
18. P. Noble, J.J. Boon, J. Wadum, in *ArtMatters, Netherlands Technical Studies in Art*, vol. 1, ed. by E. Hermans (2002), pp. 46–61
19. D.L. Pham, C. Xu, J.L. Prince, Annu. Rev. Biomed. Eng. **2**, 315–337 (2000)
20. A. Snigirev, I. Snigireva, V. Kohn, S. Kuznetsov, I. Schelokov, Rev. Sci. Instrum. **66**(12), 5486–5492 (1995)
21. M. Stampanoni, A. Groso, A. Isenegger, G. Mikuljan, Q. Chen, A. Bertrand, S. Henein, R. Betemps, U. Frommherz, P. Böhler, D. Meister, M. Lange, R. Abela, *Developments in X-Ray Tomography V*, vol. 6318 (2006), pp. U199–U212, 842
22. P. Trtik, J. Dual, D. Keunecke, D. Mannes, P. Niemz, P. Stähli, A. Kaestner, A. Groso, M. Stampanoni, J. Struct. Biol. **159**, 46–55 (2007)
23. J.D.J. van den Berg, K.J. van den Berg, J.J. Boon, Prog. Org. Coat. **41**, 143–155 (2001)
24. J.D.J. van den Berg, K.J. van den Berg, J.J. Boon, J. Chromatogr. A **950**(1–2), 195–211 (2002)
25. P. Weiss, L. Obadia, D. Magne, X. Bourges, C. Rau, T. Weitkamp, I. Khairoun, J.M. Bouler, D. Chappard, O. Gauthier, G. Daculsi, Biomaterials **24**, 4591–4601 (2003)